A Letter of Intent to PAC30: G_{Ep}/G_{Mp} with an 11 GeV electron beam

C.F. Perdrisat (co-spokesperson), T. Averett, L.P. Pentchev
College of William and Mary

V. Punjabi (co-spokesperson), M. Khandaker, C. Salgado, F.R. Wesselmann
Norfolk State University

M.K. Jones (co-spokesperson), R. Ent, H. Fenker, D. Mack, A. Radyushkin, B. Wojtsekhowski
Jefferson Lab

E.J. Brash (co-spokesperson), D. Doughty
Christopher Newport University and Jefferson Lab

E. Tomasi-Gustafsson
DAPNIA, Saclay, France

W. Boeglin, P. Markowitz, J. Reinhold
Florida International University

E. Christy, C. Keppel, V. Tvaskis
Hampton University

L. Bimbot
Institut de Physique Nucléaire, Orsay, France

A. Davidenko, Y. Goncharenko, V.I. Kravtsov, Yu. M. Melnik, and A.N. Vasiliev
Institute for High Energy Physics, Protvino, Russia

N. Piskunov, D. Kirillov, I. Sitnik, J. Mushinsky, S. Basylev, V. Slepnev and I. Slepnev
Laboratory for High Energy, JINR, Dubna, Russia

Yu. Zanesvky, S. Chernenko, and D. Fateev
Detector Research Group
Laboratory for High Energy, JINR, Dubna, Russia

G.M. Huber. Z. Papandreou

University of Regina, Canada

R. Gilman, C. Glashausser, X. Jiang, G. Kumbartzki, R. Ransome
Rutgers University

E. Frlez
University of Virginia

C. Djalali, R. Gothe, S. Strauch, D. Tedeschi
University of South Carolina

H. Voskanian, K. Egiyan, A. Ketikyan
H. Mkrtchyan, V. Tadevosyan,T. Navasardyan
Yerevan Physics Institute, Armenia

1 Introduction

In many senses, the internal structure of the nucleon is the defining problem of QCD, the fundamental theory of the strong interaction. The internal structure of the nucleon defines its mass, spin, and its interactions. The nucleon is the fundamental building block of the nucleus, and indeed it is the residual nucleon-nucleon interaction that governs all nuclear structure, in much the same way that residual interactions between atoms governs molecular structure. As such, a full and detailed quantitative understanding of the internal structure of the nucleon is a necessary precursor to extending our understanding of nuclear physics.

Based on more than a half-century of experimental and theoretical effort, we have made significant progress in our understanding of nucleon structure. At short distances, the quarks inside the nucleon are nearly unbound; this is the region of asymptotic freedom, where the quark-quark interaction is feeble. As a result, the interaction may be treated perturbatively, and the theory known as pQCD (perturbative QCD) describes a wealth of experimental data extremely well. However, at larger distances, quarks are strongly bound; this is the region of quark confinement, where QCD becomes complex, and exact quantitative calculations are exceedingly difficult.

A fundamental test of the QCD in the confinement region is the electromagnetic structure of the nucleon. In particular, measurements of the elastic electric and magnetic form factors of the proton, G_{Ep} and G_{Mp}, respectively,

at large momentum transfer, Q^2, shed new light on its internal nonperturbative structure. To this point, we have relied primarily on QCD models to attempt to describe the data. In recent years, lattice QCD has emerged as a theory which holds great promise. We note, for example, recent calculations [1, 2, 3] of the nucleon electromagnetic form factors on the lattice; while this represents a significant step forward, much work still remains to be done before meaningful quantitative comparisons between the data and unquenched lattice QCD calculations can be made.

1.1 Contributions to the Base Equipment of Hall C

Several members of the collaboration proposing this experiment in the present LOI are committed to build the focal tracking package for the SuperHMS (SHMS) spectrometer in Hall C, and are preparing a Major Research Instrumentation (MRI) proposal to the National Science Foundation to obtain the necessary funding. They are fully engaged in contributing an important part of the instrumentation of the new base equipment in Hall C, namely the SHMS.

2 Current Status of the Experimental Data

The ratio, $R_p = \mu_p G_{Ep}/G_{Mp}$, where μ_p is the proton magnetic moment, has been measured extensively over the last several decades using two experimental techniques. In the Rosenbluth separation method, one measures the angular dependence of the $e-p$ scattering cross section at a fixed value of Q^2. The results are consistent with $R_p \approx 1$ for $Q^2 < 6$ GeV^2 [4, 5, 6, 7]. In dramatic contrast, however, a series of Jefferson Lab experiments [8, 9, 10, 11] using the polarization transfer method, where one measures R_p directly by measuring the ratio of transverse to longitudinal polarizations of the recoiling proton, have revealed that the ratio decreases approximately linearly with increasing Q^2 over the same momentum range. The polarization transfer results are of unprecedented high precision and accuracy, due in large part to the small systematic uncertainties associated with the experimental technique, and cannot currently be reconciled with the Rosenbluth separation results. These results were unexpected, and have stimulated an onslaught of theoretical papers on the subject; indeed, the two main experimental papers describing the JLab results have over 500 citations combined at this time.

One possible reason for the observed discrepancy lies in the radiative corrections which are very important for Rosenbluth cross sections, but much less so for the polarization results. The LT separation technique extracts the ratio, R_p, from the ϵ dependence of the cross section at fixed Q^2. With increasing Q^2, the cross section is dominated by G_{Mp}, while the relative contribution of G_{Ep} is diminished. Hence, the ϵ dependence of the radiative correction becomes increasingly important at high Q^2. In contrast, what is measured in polarization transfer experiments is a ratio of cross sections, corresponding to longitudinal and transverse polarization, and both are affected similarly by radiative effects; it is this subtle cancellation effect that results in only an extremely weak dependence on radiative corrections. Although the G_{Ep} "crisis" has not been entirely resolved at this time, it appears likely that a combination of more careful calculations of the standard contributions to radiative corrections, and inclusion of the previously ignored two-hard-photon contribution, might fully explain it (See, for example, Refs. [12, 13]).

The third G_{Ep}/G_{Mp} experiment is now tentatively planned for late 2007; it will extend the Q^2-range from 5.6 to 8.5 GeV^2 (nominally 9 GeV^2). It might indicate that the G_{Ep}/G_{Mp} ratio is still decreasing, possibly crossing zero. The results from the first two experiments indicate clearly that we are not close to the pQCD regime, but rather in a regime dominated by soft physics (see, for example, the discussion in subsequent sections on the scaling behaviour of F_2/F_1).

3 Summary of Theoretical Efforts

To date, all theoretical models of the nucleon form factors are based on effective theories; they all rely on a comparison with existing data and their parameters are adjusted to fit the data. The much improved quality of the data from JLab has made a significant impact on theoretical models. Still, as we will see, the comparatively limited range of dynamic coverage of the form factor data results in large model uncertainties in many cases.

In the following sections, we discuss a number of distinct theoretical approaches. In some cases, these calculations could be considered to be "first principle" calculations of the form factors. In others, a more phenomenological approach is taken, in the hopes of gaining a more intuitive understanding of nucleon structure.

3.1 Relativistic Constituent Quark Models

In the constituent quark model, the nucleon consists of three constituent quarks, which are thought to be valence quarks dressed with gluons and quark-antiquark pairs that are much heavier than the QCD Lagrangian quarks. All other degrees of freedom are absorbed into the masses of these quarks. The early success of the non-relativistic constituent quark model was in describing the spectrum of baryons and mesons with correct masses[14]. However, to describe the elastic form factor data in terms of constituent quarks, it is necessary to include relativistic effects because the momentum transfers involved are up to ten times larger than the constituent quark mass.

In the earliest study of the relativistic constituent quark models (RCQM), Chung and Coester [15] calculated electromagnetic nucleon form factors with Poincaré-covariant constituent-quark models and investigated the effect of the constituent quark masses, the anomalous magnetic moment of the quarks, and the confinement scale parameter; the prediction is shown as a dotted line in Fig. 1. The agreement with the data over the range of Q^2 of the calculation is remarkable; in particular we note that the general trend of decreasing form factor ratio with increasing Q^2 is closely connected with the inclusion of relativistic effects.

Subsequently, Frank *et al.* [16] had calculated G_{Ep} and G_{Mp} in the light-front constituent quark model and predicted that G_{Ep} might change sign near 5.6 GeV^2; this predicted value is inconsistent with the current data. The calculation used the light-front nucleonic wave function of Schlumpf [17]. The light-front dynamics can be seen as a Lorentz transformation to a frame boosted to the speed of light. Under such a transformation, the spins of the constituent quarks undergo Melosh rotations. These rotations, by mixing spin states, play an important role in the calculation of the form factors. The results of their calculation are shown as the thick solid line curve in Fig. 1. The importance of this calculation lies primarily in the notion that intrinsic spin is itself a relativistic effect, and thus a comparison of the data to such calculations help us to disentangle for example the relativistic dynamics from other intrinsic nucleon structure effects.

Several calculations with the RCQM have been motivated specifically by the data from the JLab experiments [18, 19, 20, 21]. Cardarelli *et al.* [18] calculated the ratio with light-front dynamics and investigated the effects of SU(6) symmetry breaking. They showed that the decrease in the ratio with increasing Q^2 is due to the relativistic effects generated by Melosh ro-

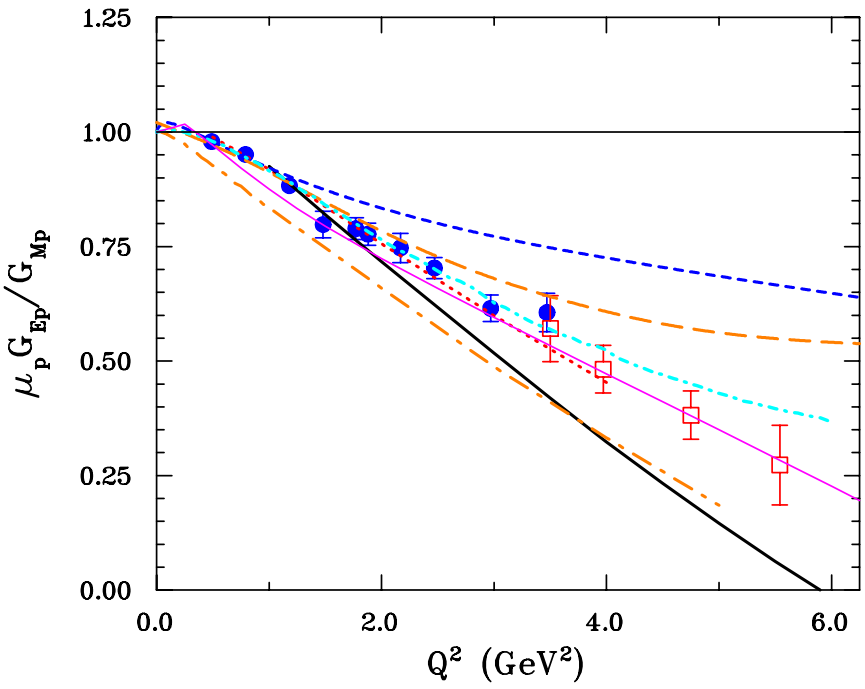

Figure 1: *Comparison of constituent quark model calculations with the data of Ref. [8](solid circles) and Ref. [9] (empty squares). The curves are: dotted [15], thick solid [16], short dot-dashed [18], dot-dashed and dashed [19], short dashed [21], and thin solid [23].*

tations of the constituent quark's spin (short dot-dashed in Fig. 1). In Ref. [19], they pointed out that within the framework of the RCQM with the light-front formalism, an effective one-body electromagnetic current, with a proper choice of constituent quark form factors, can give a reasonable description of pion and nucleon form factors. The results of their calculation with two different quark form factors are shown as the dot-dashed and dashed curves in Fig. 1. It is interesting to note that the two calculations begin to diverge significantly from one another, and from the data, with increasing Q^2. This highlights how accurate and precise data at large Q^2 can serve to further constrain such models, and thus provide a deeper understanding of the underlying structure.

De Sanctis *et al.* [20] have calculated the ratio G_{Ep}/G_{Mp} within the hypercentral constituent quark model including relativistic corrections: however, the slope of their G_{Ep}/G_{Mp} ratio is too small by a factor of $\sim$2. The chiral constituent quark model based on Goldstone-boson-exchange dynamics was used by Boffi *et al.* [21] to describe the elastic electromagnetic and weak form factors. They compute these form factors in a covariant framework using the point-form approach to relativistic quantum mechanics. The results of these calculations are shown as the short dashed curve in Fig. 1.

Miller [22] has used a model proton wavefunction, constructed using Poincaré invariance and constrained by the JLab data, to study the shape of the proton. Interestingly, Miller puts forward the idea that a nonvanishing sum of the orbital angular momentum of the quarks of the proton is indicated by non-spherical shapes. By evaluating the rest frame ground state matrix elements of spin-dependent charge density operators, he concludes that for high momentum quarks with spins aligned either parallel or anti-parallel to the proton spin, a non-spherical shape results.

Subsequently, Gross and Agbakpe [23] revisited the RCQM imposing the condition that the constituent quarks become point particles as $Q^2 \rightarrow \infty$ as required by QCD. Using a covariant spectator model which allows exact handling of all Poincaré transformations, and monopole form factors for the constituent quarks, they obtain excellent ten parameter fits to all four nucleon form factors (shown as thin solid line in Fig. 1). They conclude that the recoil polarization data can be fitted with a spherically symmetric state of three constituent quarks.

Most recently, Kvinikhidze and Miller [24] have shown that the Gross and Agbakpe model nucleon does indeed contain non-spherical shapes; they conclude that it is the use of the $spin-dependent$ density operator which is

key to revealing these features. Finally, they point out that deviations from a spherical shape are associated physically with the motion of the spin-$\frac{1}{2}$ quarks moving relativistically within the proton.

The main conclusions that we draw from the comparison of the various models to the data in Fig.1 are:

- The models are certainly beginning to diverge from one another as Q^2 increases. Thus, new accurate and precise data at large values of Q^2 will serve to severely constrain these models.

- We have seen that through a comparison of the data to the various models, and through the procedure of tuning these models to the data, we are able to gain new and important information regarding dynamical effects, as well as the underlying nucleon structure. Moreover, the availability of accurate and precise data to as large a value of Q^2 as possible helps us to disentangle these effects from one another.

G_{Ep}/G_{Mp} can also be related to the more fundamental ratio of the Pauli to Dirac form factors, $\mathrm{F}_{2p}/\mathrm{F}_{1p}$. In pQCD, where the hard scattering process dominates, one expects that this ratio should scale with Q^2, i.e. $\mathrm{Q}^2\mathrm{F}_{2p}/\mathrm{F}_{1p}$=constant. The experimental results, which are shown in Fig. 2 clearly show that we have not reached the pQCD region, as such scaling has not been observed. At the same time we note that if one instead plots the ratio $\mathrm{QF}_{2p}/\mathrm{F}_{1p}$, as shown in Fig. 3, one sees that the current data reach a constant value above $\mathrm{Q}^2 \sim 1.5$ GeV^2.

Belitzky *et al.* [25] refer to this observed scaling as "precocious", and attribute it (as does Brodsky [26]) to an extra logarithmic term from higher twist contributions that is only approximately constant in this Q^2 range. In contrast, within the context of relativistic constituent quark models, Miller and Frank [27] have shown that imposing Poincaré invariance leads to violation of the helicity conservation rule, which results in the behavior of F_{2p}/F_{1p} observed in the JLab data. We note that extending the data set to much higher Q^2, to see if the observed scaling trend continues, would indeed shed light on this interesting question.

3.2 Charge and Magnetization Densities

At low momentum transfers, one can interpret elastic electromagnetic form factors of the proton as the Fourier transforms of the charge and magnetization densities. However, this picture is complicated at larger values of Q^2,

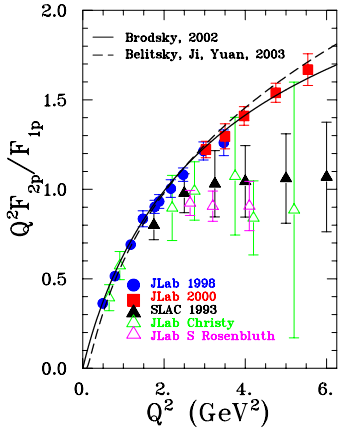

Figure 2: *The ratio Q^2F_2/F_1 extracted from the JLab data, compared to two recent pQCD predictions, by Belitzky et al. [25] and Brodsky [26].*

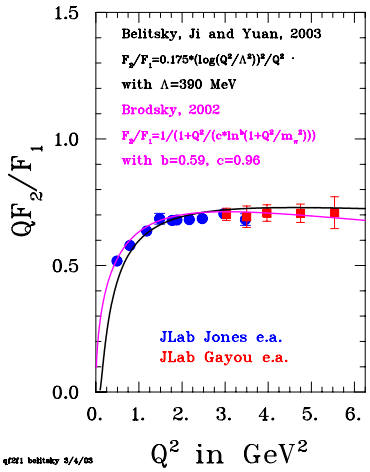

Figure 3: *The ratio QF_2/F_1, compared to the same pQCD predictions, by Belitzky et. al. [25] and Brodsky [26].*

because of nucleon recoil and Lorentz contraction effects. Still, a great deal of intuitive information may be gained from the extraction of charge and magnetization densities from the available form factor data, even though there remains some model dependency in the results.

The charge and magnetization densities of the proton in coordinate space are given, respectively, by

$$\rho_{ch}(r) = \frac{2}{\pi}\int_0^\infty k^2 j_0(kr)\tilde{\rho}_{ch}(k)dk, \quad (1)$$

$$\rho_m(r) = \frac{2}{\pi}\int_0^\infty k^2 j_0(kr)\tilde{\rho}_m(k)dk. \quad (2)$$

In the typical non-relativistic method, one assumes that $k \to Q$ and $\tilde{\rho}(Q) \to G(Q^2)$. However, this method leads to unreasonable and/or unphysical densities in many instances.

For example, while early experiments at low to moderate Q^2 seemed to indicate that the proton form factors both followed a dipole form, the Fourier transform of a dipole form factor produces an exponential charge distribution, with a clearly unphysical cusp at the origin. A Gaussian charge density is more plausible physically, and has been shown to give a reasonable fit to the

form factor data once Lorentz contraction effects are taken into account [28]. However, while this and other models offer plausible radial densities, they are not innately compatible with the scaling behaviour predicted by pQCD at very large Q^2.

Using the currently available data on all four elastic nucleon form factors, Kelly [29] has extracted charge and magnetization densities for the nucleon. The prescription that is followed in order to account for failures in the non-relativistic inversion method is to apply a boost from the Breit frame with momentum $q_B = Q$ to the rest frame, which results in a reduced spatial frequency, given by

$$k^2 = \frac{Q^2}{1+\tau}, \tag{3}$$

where $\tau = \frac{Q^2}{4m_p^2}$. In addition, one parametrizes the momentum dependent charge and magnetizations according to

$$\tilde{\rho}_{ch}(k) = G_E(Q^2)(1+\tau)^{\lambda_E}, \tag{4}$$

$$\mu\tilde{\rho}_m(k) = G_M(Q^2)(1+\tau)^{\lambda_M}. \tag{5}$$

The parameters, λ_E and λ_M, take on, in principle, different values within different models. Kelly notes that $\lambda_E = \lambda_M = 2$ satisfies the pQCD scaling constraint at large Q^2. Moreover, the calculations indicate that one is more sensitive to the specific choice of $\lambda_{E,M}$ at large radius/low Q^2. Thus, there is only moderate model dependence in the extracted charge and magnetization densities at small radius/high Q^2.

To further assess the model dependence in the extraction, Kelly uses the technique of linear expansions in complete sets of basis functions that are capable of describing any plausible radial distribution, without any *a priori* constraints on its shape. In particular, this allows one to estimate the uncertainty in the fitted density due to both the statistical quality of the data, as well as on the limited range of Q^2 over which one has accurate and precise data.

The extracted charge and magnetization densities are shown in Figure 4. The charge density is significantly broader than the magnetization because G_{Ep} is softer than G_{Mp}, falling more rapidly with respect to Q^2. In particular, though, we note that the uncertainty in the densities near the origin is dominated by a lack of knowledge of the form factors at large Q^2. New high precision data at large Q^2 would serve to significantly reduce the uncertainty

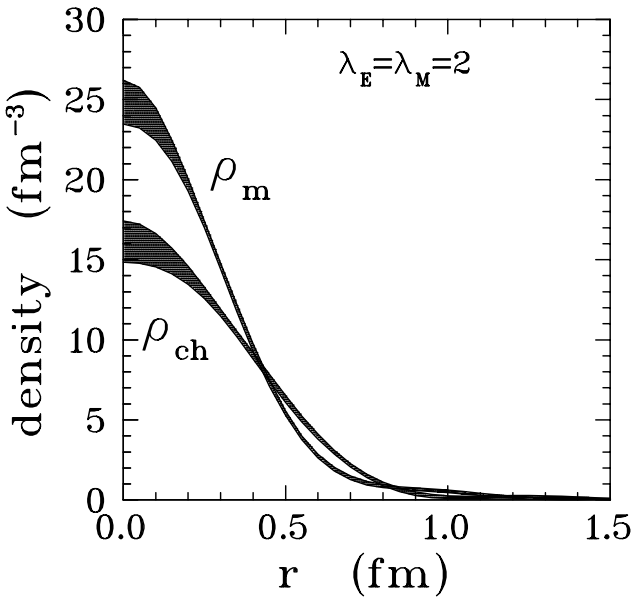

Figure 4: *Charge and magnetization densities of the proton obtained by [29].*

band shown in the calculation near the origin. Indeed, if the form factor ratio were to continue to fall linearly up to $Q^2 \sim 13\ GeV^2$, one would expect the charge density to "turn over" such that it had a positive slope on its approach to the origin, signaling a "hole" in the charge density at the core of the proton. Of course, the slope should ultimately be zero at $r = 0$, a feature which is internally consistent with $G_{Ep}/G_{Mp} \approx constant$ as $Q^2 \to \infty$.

3.3 Generalized Parton Distributions

The Generalized Parton Distributions (GPDs), introduced nearly a decade ago, represent a framework within which hadrons are described in terms of quark and gluonic degrees of freedom (See, for example, Refs. [30, 31, 32, 33, 34]) . They combine together the concepts of form factors, parton densities, and distribution amplitudes, and as such serve as an extremely useful tool in studies of hadronic structure.

It turns out that the elastic electromagnetic form factors of nucleons are related to moments of the GPDs and therefore offer important constraints

on the GPDs themselves, and thus in turn constrain our description of the nucleon's structure. The nucleon Dirac, F_1, and Pauli, F_2 form factors are the zeroeth moments of the $H(x,t)$ and $E(x,t)$ GPDs :

$$F_1(t) = \sum_q e_q F_1^q(t) \qquad F_2(t) = \sum_q e_q F_2^q(t) \tag{6}$$

$$F_1^q(t) = \int_{-1}^{+1} dx H^q(x,\xi,t) \qquad F_2^q(t) = \int_{-1}^{+1} dx E^q(x,\xi,t) \tag{7}$$

in which q are the quark flavors. In an early use of GPDs to describe the nucleon form factor, F_1, Radyushkin [30] parametrized the H GPD with a Gaussian form and was able to fit the existing data with only a single parameter. When precision data from the JLab experiments for F_2/F_1 up to Q^2=3.5 GeV^2 became available, Afanasev [31] extended the approach of Radyushkin and included a determination of the E GPD. This was the first attempt to extract information on the angular momentum of the valence quarks and indicated a need to measure F_2/F_1 to large Q^2 in order to determine the x dependence of the E GPD. Using the most recent JLab data for F_2/F_1 for the proton up to Q^2=5.6 GeV^2 and for the neutron F_2/F_1 up to $Q2$=1.5 GeV^2, two theoretical groups [33, 34] have fitted H and E GPDs to the existing nucleon form factor data.

The form factors are independent of the skewness, ξ, which simplifies the GPD integrals, in contrast to deeply virtual exclusive (DVE) reactions. While GPD formalism for DVE reactions is limited to low t, the GPD formalism for the form factors is applicable to high t, and thus form factor measurements at high t (large Q^2) are ideally complementary to the DVE experiments. The invariant t depends on both the longitudinal and transverse components of the momentum transferred to the nucleon. Therefore, form factor measurements at high t allow unique access to the small transverse momentum structure of the nucleon.

By introducing non-forward parton densities :

$$\mathcal{H}^q(x,t) = H^q(x,0,t) + H^q(-x,0,t) \tag{8}$$

$$\mathcal{E}^q(x,t) = E^q(x,0,t) + E^q(-x,0,t) \tag{9}$$

the integrals in Eqns. 6 and 7 can be reduced to integrals over $0 < x < 1$. The $\mathcal{H}^q(x,t)$ are equal to the valence quark densities, $u_v(x)$ and $d_v(x)$, in the limit of $t \to 0$. But the $\mathcal{E}^q(x,t=0)$ cannot be directly expressed in terms of any known parton distribution. New information about the transverse

momentum distribution of the quarks in the nucleon is contained in $\mathcal{E}^q(x, t = 0)$. Just as the normalization integrals for the $\mathcal{H}^q(x, t)$ are related to the charge of the quarks, the normalization integrals for $\mathcal{E}^q(x, t = 0)$ must equal their anomalous magnetic moment.

Burkhardt [35] introduced the concept that the Fourier transform of the GPDs at $\xi = 0$ describes the distribution of partons in the transverse plane. The form factors are non-forward matrix elements of the current operator, and describe how the charge (i.e. the forward matrix element of the same operator) is distributed in position space. By analogy, as off-forward matrix elements, the GPDs contain information about how the parton distribution functions (PDFs) are distributed in position space. While conventional PDFs contain no information about the spatial distribution of partons, if one knows the GPDs for $\xi = 0$, one can simultaneously determine the longitudinal momentum and transverse position of partons in the target nucleon. As an example, in Fig. 5, we show calculations from [34] of the up and down valence quark densities in the proton extracted from form factor data as functions of transverse position, for various values of x.

One of the most interesting constraints that nucleon elastic form factor data at large Q^2 can provide relates to the issue of the various contributions from quarks, gluons, and orbital angular momentum to the total angular momentum of the nucleon.

A quark of flavor q in the nucleon has a total angular momentum, J^q, which is related to the GPD's H^q and E^q by the sum rule [36] :

$$2J^q = \int_{-1}^{1} x\{H^q(x, 0, 0) + E^q(x, 0, 0)\}dx \tag{10}$$

In Ref. [33], $\mathcal{H}^q(x, t)$ is parametrized in modified Regge form as

$$\mathcal{H}^q(x, t) = q_v(x)x^{-\alpha_1(1-x)t} \tag{11}$$

The $q_v(x)$ are the known parton distributions, so $\mathcal{H}^q(x, 0, 0)$ is simply given by $q_v(x)$. $\mathcal{E}^q(x, 0, 0)$ is unknown and, in Ref. [33], $\mathcal{E}^q(x, t)$ is parametrized as:

$$\mathcal{E}^q(x, t) = \frac{\kappa_q}{N_q}(1 - x)^{\eta_q} q_v(x)x^{-\alpha_2(1-x)t} \tag{12}$$

in which N_q is a normalization fixed by $\kappa_q = \int_0^1 \mathcal{E}^q(x, 0)dx$. Fitting the nucleon form factor data determines the coefficient α_1 of $\mathcal{H}^q(x, t)$ and the coefficients, α_2, η_u and η_d in $\mathcal{E}^q(x, t)$. A good fit is obtained to the nucleon

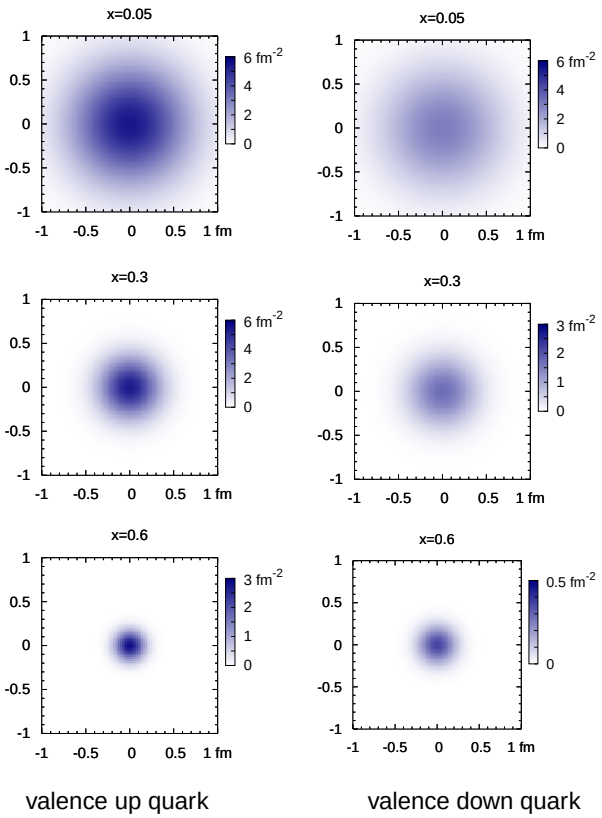

Figure 5: *Transverse valence quark densities extracted from form factor data (From Ref. [34])*

magnetic form factors and the ratio of the nucleon G_E/G_M has a better fit with the extra η_u and η_d parameters. The η_u and η_d parameters define the large x behavior of $\mathcal{E}^q(x,t)$ which is determined from the large t dependence of F_2^p/F_1^p.

Neglecting the sea quark contribution, the contribution of the u and d valence quarks to the total angular momentum can be calculated. Ref. [33] calculates $2J^u = 0.63$ and $2J^d = -0.06$ which agree with quenched lattice QCD calculations. The intrinsic spin contribution of the valence quark, Δq_v, is known from the PDFs, so the orbital angular momentum of the quark can be calculated according to $2L^q = 2J^q - \Delta q_v$. Over the coming years, with the projected availability of reliable unquenched lattice QCD calculations, it will be desirable to have elastic form factor data at the highest Q^2 possible so that meaningful comparisons can be made between lattice QCD and GPD-based calculations.

4 The Recoil Polarization Method

The relationship between the Sachs electromagnetic form factors and the degree of polarization transfer in ${}^1H(\vec{e},e'\vec{p})$ scattering was first developed by Akhiezer and Rekalo [37], and later discussed in more detail by Arnold, Carlson, and Gross [38].

For single photon exchange, the transferred polarization can be written in terms of the Sachs form factors:

$$P_n = 0 \tag{13}$$

$$\pm h P_l = \pm h \left(\frac{E_e + E_e'}{M}\right) \frac{\sqrt{\tau(1+\tau)}\, G_{Mp}^2(Q^2)\, \tan^2\frac{\theta_e}{2}}{G_{Ep}^2(Q^2) + \frac{\tau}{\epsilon_\gamma} G_{Mp}^2(Q^2)} \tag{14}$$

$$\pm h P_t = \mp h \frac{2\sqrt{\tau(1+\tau)}\, G_{Ep}\, G_{Mp}\, \tan\frac{\theta_e}{2}}{G_{Ep}^2(Q^2) + \frac{\tau}{\epsilon_\gamma} G_{Mp}^2(Q^2)} \tag{15}$$

where the $\pm$ stands for the two possible orientations of the electron beam helicity.

For each Q^2, a single measurement of the azimuthal angular distribution of the proton scattered in a secondary target (described later) gives both the

longitudinal and transverse polarizations. Combining Eq. 14 and 15 gives:

$$\frac{G_{Ep}}{G_{Mp}} = -\frac{P_t}{P_l}\frac{(E_e + E'_e)}{2M}\tan\frac{\theta_e}{2}, \tag{16}$$

thus the ratio of electric to magnetic form factors of the proton is obtained directly from a simultaneous measurement of the two recoil polarization components. The kinematic factors in Eq. 16 are typically known to a precision far greater than the statistical precision of the recoil polarization components.

4.1 Focal Plane Polarimetry

The azimuthal distribution of the protons which undergo a second scattering in the analyzer is dependent upon the proton polarization due to the spin-orbit part of the strong nuclear force [39]. The degree of polarization is directly related to the asymmetry of this angular distribution by:

$$N_p^{\pm}(\theta,\phi) = N_p^{\pm}(h=0)\Big[1+(\pm hA_y(\theta)P_t^{fp}+a_i)\sin\phi+(\pm hA_y(\theta)P_l^{fp}+b_i)\cos\phi\Big], \tag{17}$$

where $N_p^{\pm}(h=0)$ is the number of protons incident on the polarimeter, h is the helicity, and a_i and b_i are the instrumental asymmetries. Empirically, the analyzing power, A_y, is the amplitude of the asymmetry resulting from the scattering of a particle with polarization, P_y, i.e. $A_y = \frac{A}{P_y}$. It is important to note that in this experiment to extract P_t^{fp} and P_l^{fp}, we take the **difference** in angular distributions of positive and negative electron helicities, and thus are completely insensitive to the instrumental asymmetries.

The crucial feature of the polarimeter is its coefficient of merit (COM), defined as COM$=\int_{\vartheta_{min}}^{\vartheta_{max}}\epsilon(\vartheta)A_y(\vartheta) \sim \epsilon A_y^2$, where $\epsilon(\vartheta)$ is the differential fraction of events scattered in the analyzer at polar angle ϑ, and $A_y(\vartheta)$ is the corresponding analyzing power. The data are binned in ϑ, and a value of $G_{Ep}/G_{Mp}(\vartheta)$ obtained for each bin; the weighted average is the result of the experiment.

4.2 Spin Precession

Typically, elastic *ep* events are identified by using coincidence detection of both electron and proton. In this experiment, the electron will be detected using the BigCal lead-glass detector array (as will be the case in the upcoming Gep-III (JLab E04-108) experiment in Hall C), and the proton will be

detected with the planned SuperHMS (SHMS) spectrometer. As the proton travels through the SHMS, its spin precesses due to the interaction of the magnetic moment of the proton with the magnetic elements of the SHMS, which consists of a horizontal bending magnet, followed by a series of quadrupole magnets as well as the principal vertical bend dipole magnet.

The proton polarization at the spectrometer focal plane is related to its polarization at the target by a spin matrix:

$$\begin{pmatrix} \mathbf{P_n^{fp}} \\ \mathbf{P_t^{fp}} \\ P_l^{fp} \end{pmatrix} = \begin{pmatrix} S_{nn} & \mathbf{S_{nt}} & \mathbf{S_{nl}} \\ S_{tn} & \mathbf{S_{tt}} & \mathbf{S_{tl}} \\ S_{ln} & S_{lt} & S_{ll} \end{pmatrix} \begin{pmatrix} P_n^{tar} \\ \mathbf{P_t^{tar}} \\ \mathbf{P_l^{tar}} \end{pmatrix}$$

The focal plane polarimeter measures only the transverse and normal, P_t^{fp} and P_n^{fp}, components of the proton polarization. The spin matrix is calculated using a model of the spectrometer with the differential-algebra-based transport code COSY. Details are given in Ref. [11] regarding the method for extracting the target polarizations from knowledge of the spin matrix and measurement of the $N(\theta, \phi)$ distributions. For a standard QQQD magnet spectrometer, the spin matrix components, S_{nt} and S_{tl}, are almost zero when averaged over the phase space. The addition of the horizontal bender in front of the SHMS QQQD magnet system creates a potential complication, since the phase space averaged S_{nt} and S_{tl} will now have a non-zero value.

The effect of the horizontal bending magnet is to mix the transverse and longitudinal components, P_t^{tar} and P_l^{tar} of the outgoing elastic proton. After the horizontal bender, the transverse and longitudinal components are

$$P_t^{hb} = P_l^{tar} \sin\phi_{hb} + P_t^{tar} \cos\phi_{hb}, \quad (18)$$

$$P_l^{hb} = P_l^{tar} \cos\phi_{hb} - P_t^{tar} \sin\phi_{hb}, \quad (19)$$

in which $\phi_{hb} = \kappa_p \gamma \theta_{bend}^H$ is the precession angle of the horizontal bending magnet. The bend angle of the magnet, θ_{bend}^H, is 3°. For $Q^2 = 10.5$ and 13 GeV^2, $\gamma = 7.0$ and 8.4 which gives $\phi_{hb} = 37.5°$ and 45.1°, respectively. For spin transport after the horizontal bender to the SHMS focal plane, we will ignore the quadrupoles and treat the dipole magnet as a simple dipole. Of course in the actual experiment, we will use the full calculation of the spin matrix, a technique which has been firmly established in the previous JLab experiments, and which is well understood.

The transverse and normal components, P_t^{fp} and P_n^{fp}, at the SHMS focal

plane are

$$P_t^{fp} = P_t^{hb} = P_l^{tar}\sin\phi_{hb} + P_t^{tar}\cos\phi_{hb}, \quad (20)$$

$$P_n^{fp} = P_l^{hb}\sin\phi_d = (P_l^{tar}\cos\phi_{hb} - P_t^{tar}\sin\phi_{hb})\sin\phi_d. \quad (21)$$

Since P_t^{hb} is unchanged by the simple dipole magnet and P_l^{hb} is rotated by the dipole's precession angle, $\phi_d = \kappa_p\gamma\theta_{bend}^D$. With the dipole's bend angle, θ_{bend}^D, equal to 18.4°, this gives $\phi_d = 229.7°$ and 276.5°, which is in general very favourable for this experiment, especially at the largest Q^2 value considered.

For a simple estimate of the uncertainty on the target polarization components one rewrites the equations as:

$$P_t^{tar} = P_t^{fp}\cos\phi_{hb} - P_n^{fp}\frac{\sin\phi_{hb}}{\sin\phi_d} \quad (22)$$

$$P_l^{tar} = P_t^{fp}\sin\phi_{hb} + P_n^{fp}\frac{\cos\phi_{hb}}{\sin\phi_d} \quad (23)$$

The fractional uncertainty on P_t^{fp} and P_n^{fp} is $\sqrt{\frac{2}{NA^2}}$ where A is the analyzing power and N is the number of protons which scatter in the analyzer in a given angular range. Thus, the uncertainties on the target polarizations are

$$(\Delta P_t^{tar})^2 = (\Delta P_t^{fp})^2\cos^2\phi_{hb} + (\Delta P_n^{fp})^2\frac{\sin^2\phi_{hb}}{\sin^2\phi_d}, \quad (24)$$

$$(\Delta P_l^{tar})^2 = (\Delta P_t^{fp})^2\sin^2\phi_{hb} + (\Delta P_n^{fp})^2\frac{\cos^2\phi_{hb}}{\sin^2\phi_d}. \quad (25)$$

Since $\Delta P_t^{fp} = \Delta P_n^{fp} = \sqrt{\frac{2}{NA^2}}$, the equations can be rewritten as

$$(\Delta P_t^{tar})^2 = \frac{2}{NA^2}(\cos^2\phi_{hb} + \frac{\sin^2\phi_{hb}}{\sin^2\phi_d}) \quad (26)$$

$$(\Delta P_l^{tar})^2 = \frac{2}{NA^2}(\sin^2\phi_{hb} + \frac{\cos^2\phi_{hb}}{\sin^2\phi_d}) \quad (27)$$

For $Q^2 = 13$ GeV^2, $\sin\phi_d \approx 1$, and thus $\cos^2\phi_{hb} + \frac{\sin^2\phi_{hb}}{\sin^2\phi_d} \approx 1$ and the uncertainties on the target polarizations are approximately equal to those at the focal plane. For $Q^2 = 10.5$ GeV^2, $\sin\phi_d \approx 0.76$, the uncertainties on the target polarizations are multiplied by ≈ 1.30 for both ΔP_t^{tar} and ΔP_l^{tar}. Without the horizontal bending magnet only ΔP_l^{tar} would be increased by the precession in the dipole magnet.

5 The Experiment

5.1 Basic Apparatus

This experiment will use the Super High Momentum Spectrometer (SHMS) in Hall C to detect the recoiling proton, and the BigCal lead glass calorimeter to detect the scattered electron. The focal plane in the SHMS will be equipped with the Focal Plane Polarimeter that is currently being installed in the HMS spectrometer in Hall C for the Gep-III experiment. Therefore, this experiment requires no new equipment beyond the base equipment planned for the Hall C 12 GeV upgrade.

5.1.1 The Super High Momentum Spectrometer

The SHMS bends charged particles in both the horizontal and vertical plane; it consists of horizontal 3° bending magnet, whose primary function is to allow access to small scattering angles, followed by three quadrupoles, and finally one vertical bend dipole magnet. Its angular acceptance is approximately 3.5 msr. The angular resolution is 2 mr and the momentum resolution is approximately 2×10^{-3}. The momentum and angular resolutions are perfectly adequate for this experiment. The highest momentum accepted by the SHMS is 10.4 GeV/c, corresponding to Q^2=18 GeV^2; the vertical bend angle of the SHMS is 18.4°.

As described in the previous section, favorable precession angles are crucial to obtain the ratio G_{Ep}/G_{Mp} with small uncertainty. For the Q^2 range considered in this experiment (10 GeV^2 $< Q^2 <$ 14 GeV^2), the precession angles are very favourable.

5.1.2 The Focal Plane Polarimeter

This experiment requires the installation of a Focal Plane Polarimeter (FPP) in the focal plane area of the SHMS. As shown in Fig. 6, the design of the focal plane detection system for the SHMS has been planned from the beginning to be able to incorporate the FPP which is currently being installed in the HMS in Hall C for the Gep-III experiment. The analyzer of the FPP is divided into two blocks of CH_2, each 55 cm thick. The incoming proton trajectories will be reconstructed from using the SHMS focal plane drift chambers. Outgoing trajectories of scattered particles in either of the two analyzers are reconstructed using the FPP drift chambers.

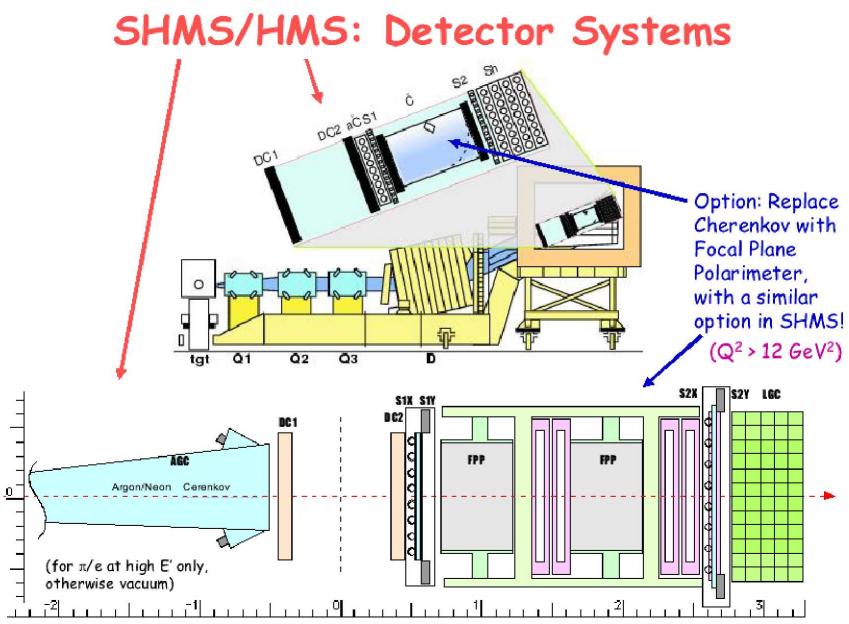

Figure 6: *Schematic Drawing of the planned SHMS focal plane detection package.*

The FPP has been designed as a unit in a sturdy frame, to facilitate its installation and removal. It will be required for this experiment that a basic underlying structure be built to support the FPP frame itself within the SHMS detector hut, just as has been done for the FPP in the HMS.

For the purposes of determining the polarimeter COM for calculating projected uncertainties, the differential scattering fraction has been estimated from a full Geant3-based simulation of the polarimeter. Previous results obtained for the scattering fraction from this simulation are in good agreement with the results of previous experiments, and thus we are confident in our estimates for this new experiment. In Fig. 7, we show the currently available maximum analyzing power data from the previous JLab experiments, as well as from measurements at Dubna[40] for CH_2, and at Saclay[41] and Moscow[42] for carbon. A combined analysis[40] of the carbon and CH_2 data showed that empirically, the maximum analyzing power is proportional

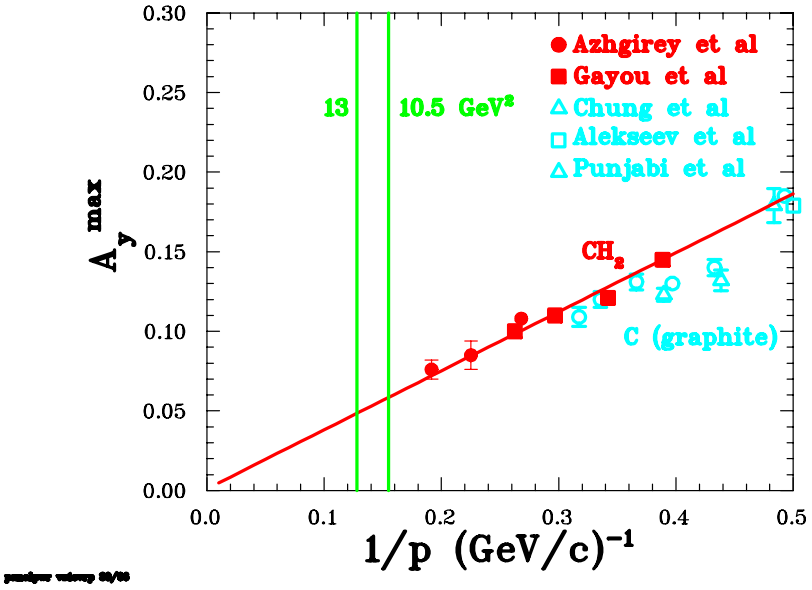

Figure 7: *Maximum carbon/CH_2 analyzing power data.*

to $1/p$ over a large range of momenta. Moreover, the shape of the analyzing power curve as a function of transverse momentum (which is proportional to the polar angle, ϑ) is largely independent of momentum, as well, with the analyzing power reaching a maximum value at $p_t \simeq 0.3$ GeV/c. We have extrapolated the linear fit to the data into the region of proton momenta which correspond to this experiment, and have used these values to estimate the average analyzing powers. We note that this is probably a somewhat *pessimistic* scenario, as it is quite likely that the maximum analyzing power will be larger than the $1/p$ extrapolation.

5.1.3 BigCal Calorimeter

Essential to this experiment is solid angle matching, which means that for each kinematics the solid angle of the electron detector must match the fixed solid angle of the proton detector, which is the SHMS. With a beam energy of 8.8-11.0 GeV, the kinematics of this experiment are such that the electron scattering angle is larger than the proton recoil angle, and therefore the Jacobian for the electron is larger than 1, and hence the solid angle for the electron detector must be larger than that of the proton detector.

Of course, the situation here is exactly the same as for the upcoming Gep-III experiment in Hall C, for which a new large lead glass calorimeter array (BigCal) has been constructed (See Fig. 8). This is the ideal detector for the electron in this experiment as well, as no modifications will be necessary.

BigCal consists of 32 columns times 32 rows of 3.8×3.8 cm^2 bars of Protvino lead glass blocks at the bottom, and 30 columns times 24 rows of 4.0×4.0 cm^2 from RCS (Yerevan blocks) placed on the top. The total frontal area is thus 2.63 m^2. At a distance of 10.0 m away from the target, the detector offers a solid angle of 26 msr to the electrons of the *ep* reaction, which is adequate for all of the kinematics of this experiment. The pulse height from every lead glass bar is digitized. In addition, after splitting in the multiplexer/amplifier circuit, a copy of the original signal is added in groups of eight channels for timing purposes, as well as for constructing the calorimeter trigger. The timing information helps distinguish noise from true charge sharing. Interpolation over the charge sharing in neighboring bars is expected to improve the position resolution from the canonical $d/\sqrt{12}$ ~1.2 cm, where d is the bar's transverse size, to about 0.5 cm. At a 10 m distance from the target, this corresponds to an angular resolution of approximately 0.5 mr; this is far better than is needed for this experiment, given the projected angular resolution of the SHMS ($\sim$ 2 mr).

5.2 Measurements

In Tab. 1, we present a summary of the kinematic points that have been chosen. In the appendix, we include further discussion of the various kinematic choices that were also evaluated. There are several features that are worth noting:

- At a Q^2 value of 6 GeV^2, the electron scattering angle is approximately the same as for the Q^2=13 GeV^2 point. Thus, this control point could be taken in a short amount of time, and it does not require that the calorimeter be moved to a third position in Hall C.

- While in principle all kinematics considered here can be reached using a beam energy of 8.8 GeV, beyond $Q^2 \sim 12$ GeV^2, electron solid angle matching considerations as well as the overall cross section dependence with energy favour a 11.0 GeV beam energy.

In Tab. 2, we show projected uncertainties and beam times for all of the kinematics considered. In our opinion, the 120 days of beam time required

Figure 8: *The BigCal Calorimeter.*

Q^2	E_e	θ_e	$E_{e'}$	θ_p	p_p	$d\sigma/d\Omega_e$	ϵ	χ	$\Delta\Omega_e$
GeV^2	GeV	deg	GeV	deg	GeV/c	cm^2/sr		deg	msr
6	6.6	30	3.4	25	4.03	1.1×10^{-35}	0.72	145.4	6
10.5	8.8	35.5	3.20	16.7	6.47	3.5×10^{-37}	0.55	229.7	17
13	11.0	31.3	4.07	15.7	7.81	1.6×10^{-37}	0.58	276.5	16

Table 1: *The proposed kinematics. Assumed spectrometer solid angles: 7 msr for HMS, 3.5 msr for SHMS. Assumed beam characteristics: 75 μA, 85% polarization. Assumed target: 30 cm LH_2.*

Q^2	E_e	COM	absolute $\Delta(G_{Ep}/G_{Mp})^*$	time
GeV^2	GeV			days
6.0	**6.6**	**3.9×10^{-3}**	**0.049**	**4**
10.5	**8.8**	**1.5×10^{-3}**	**0.13**	**30**
13.0	**11.0**	**1.1×10^{-3}**	**0.16**	**60**

Table 2: *Absolute uncertainties (not including systematics), and times required. The assumed beam intensity and electron beam polarization are 75 μA and 0.85, respectively. The target length is 30 cm, and the SHMS solid angle is 3.5 msr.*
* *Note that the increase in the error bar due to precession in the horizontal bender has already been included in this estimate. See the Appendix for further details.*

to acquire a data point at Q^2=14 GeV^2 (see Appendix) eliminates this from consideration at this time. At the same time, extending these measurements to the highest reasonable Q^2 value possible strongly motivates using the SHMS spectrometer to make a measurement at Q^2=13 GeV^2. As the focal plane polarimeter must be relocated to the SHMS for this measurement, then logistics dictate that we carry out all measurements using the SHMS. Considering that Gep-III will obtain a point at Q^2=8.5 GeV^2, we opt for an additional point in this experiment at Q^2=10.5 GeV^2, which essentially is half way between the Gep-III data point and our highest Q^2 data point. In addition, a control point at Q^2=6 GeV^2, requiring only 4 days of beam time, seems very reasonable.

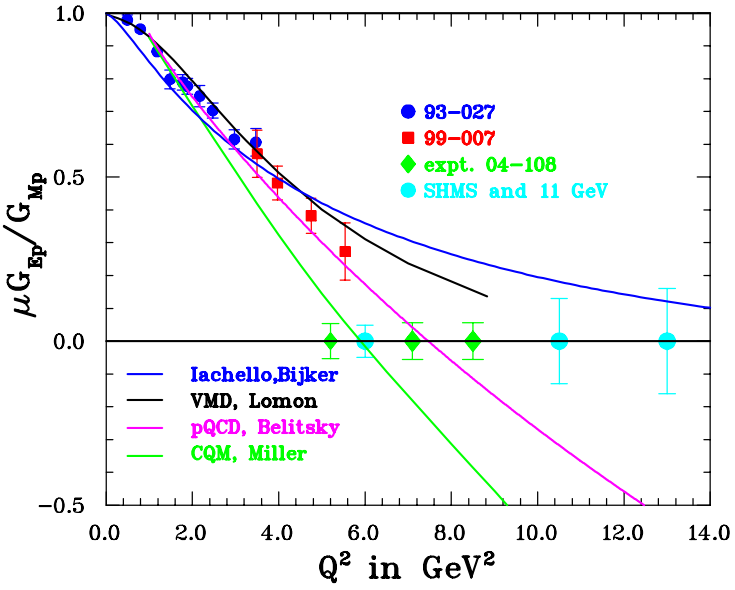

Figure 9: *Previous and projected data for the proton form factor ratio, along with a number of theoretical predictions*

The total beam time to be requested for these three new data points is approximately 94 days. In Fig. 9, we summarize the currently available data for the proton form factor ratio, together with projected data from Gep-III, and of course for this experiment. We alo include the current projections from a range of theoretical models. In addition to the models discussed previously, we also show two phenomenological Vector Meson Dominance (VMD) inspired calculations, one by Lomon [43], and another by Bijker and Iachello [44]. It seems clear that data from the experiment will provide severe constraints on these and other models of this fundamental quantity.

We close by quoting the authors of the pCDR document for the 12 GeV JLab upgrade:

> "The JLab 12 GeV Upgrade will support a great leap forward in our knowledge of hadron structure through major programs in three areas: nucleon form factors at large Q^2, valence quark structure, and deep exclusive scattering."

We feel that the proposed experiment represents an opportunity which is in fact unique in the world to provide data on the proton form factor ratio at

large Q^2, an essential ingredient in our understanding of the internal structure of hadrons.

6 Appendix

In the process of evaluating the merits of various kinematic arrangements for this experiment, an array of choices were considered. In Tab. 3, we present a summary of the possible kinematic points that have been considered, along with the spectrometer characteristics. Of course, using the existing HMS spectrometer to detect the recoil proton is certainly a reasonable option to consider, and so we have included also in this table configurations which use the HMS spectrometer. Referring to the table, we note that the largest value of Q^2 which can be reached with the HMS is 12 GeV^2. The limiting factor is of course the maximum momentum of the spectrometer. It is also important to note that in these kinematics, the spin precession (χ=350°) is not favourable. At Q^2=9 GeV^2, we note that the ϵ value of this point is quite different than for the data point at comparable Q^2 in Gep-III (ϵ=0.24 at 6 GeV beam energy). So, this would provide an interesting commentary on the possible effect of two-photon and other radiative corrections, which are thought to have potentially some ϵ dependence.

In Tab. 4, we show projected uncertainties and beam times for all of the kinematics considered, along with the FPP coefficient of merit.

References

[1] M. Göeckler *et al.*, Phys. Rev. D **71**, 034508 (2005).

[2] H.H. Matevosyan, G.A. Miller, and A.W. Thomas, Phys. Rev. C **71**, 055204 (2005).

[3] C. Alexandrou, G. Koutsou, J.W. Negele, and A. Tsapalis, [arXiv: hep-lat/0605017], May 2006.

[4] R.C. Walker *et al.*, Phys. Rev. D **49**, 5671 (1994).

[5] L. Andivahis *et al.*, Phys. Rev. D **50**, 5491 (1994).

[6] M.E. Christy *et al.*, Phys. Rev. C **70**, 015206 (2004).

FPP	Q^2	E_e	θ_e	$E_{e'}$	θ_p	p_p	$d\sigma/d\Omega_e$	ϵ	χ	$\Delta\Omega_e$
spectro	GeV^2	GeV	deg	GeV	deg	GeV/c	cm^2/sr		deg	msr
HMS	6	6.6	30	3.4	25	4.03	1.1×10^{-35}	0.72	187	10.8
HMS	9.0	8.8	29.3	4.004	20.2	5.66	1.4×10^{-36}	0.67	274	11
HMS	10.5	8.8	35.5	3.205	16.7	6.47	3.5×10^{-37}	0.55	312	56
HMS	12	8.8	44.2	2.41	13.3	7.27	0.8×10^{-37}	0.41	350	66
HMS	12	11.0	28.2	4.61	17.4	7.27	3.3×10^{-37}	0.64	350	18
SHMS	6	6.6	30	3.4	25	4.03	1.1×10^{-35}	0.72	145.4	6
SHMS	9.0	8.8	29.3	4.00	20.5	5.66	1.4×10^{-36}	0.67	201.6	8.5
SHMS	10.5	8.8	35.5	3.20	16.7	6.47	3.5×10^{-37}	0.55	229.7	17
SHMS	12	8.8	44.2	2.77	13.3	7.27	0.85×10^{-37}	0.27	259.0	37
SHMS	12	11.0	28.2	4.61	17.4	7.27	3.3×10^{-37}	0.64	259.0	10.5
SHMS	13	11.0	31.3	4.07	15.7	7.81	1.6×10^{-37}	0.58	276.5	16
SHMS	14	8.8	66.0	1.34	12.1	8.35	0.1×10^{-37}	0.19	295.3	157
SHMS	14	11.0	34.9	3.54	14.0	8.35	0.7×10^{-37}	0.50	295.3	23

Table 3: *Kinematics proposed, updated COM and spectrometer characterisitics. Assumed spectrometer solid angles: 7 msr for HMS, 3.5 msr for SHMS. Assumed beam characteristics: 75 μA, 85% polarization. Assumed target: 30 cm LH_2.*

Q^2	E_e	FPP	COM	Horiz. Bender	$\Delta(G_{Ep}/G_{Mp})^*$	time
GeV^2	GeV	spectro		Factor		days
6.0	6.6	HMS	3.9×10^{-3}		0.033	4
9.0	8.8	HMS	2.0×10^{-3}		0.047	30
10.5	8.8	HMS	1.5×10^{-3}		0.079	30
12.0	8.8	HMS	1.2×10^{-3}		0.12	60
12.0	11.0	HMS	1.2×10^{-3}		0.12	60
6.0	**6.6**	**SHMS**	$\mathbf{3.9 \times 10^{-3}}$	**1.15**	**0.049**	**4**
9.0	8.8	SHMS	2.0×10^{-3}	1.70	0.11	30
10.5	**8.8**	**SHMS**	$\mathbf{1.5 \times 10^{-3}}$	**1.30**	**0.13**	**30**
12.0	8.8	SHMS	1.2×10^{-3}	1.01	0.12	60
12.0	11.0	SHMS	1.2×10^{-3}	1.01	0.12	60
13.0	**11.0**	**SHMS**	$\mathbf{1.1 \times 10^{-3}}$	**1.00**	**0.16**	**60**
14.0	8.8	SHMS	0.9×10^{-3}	1.06	0.20	120
14.0	11.0	SHMS	0.9×10^{-3}	1.06	0.16	120

Table 4: *Absolute uncertainties (not including systematics), and times required. The assumed beam intensity and electron beam polarization are 75 μA and 0.85, respectively. The target length is 30 cm, and the SHMS solid angle is 3.5 msr.*

* *Note that for data points using the SHMS, the increase in the error bar due to precession in the horizontal bender has been included.*

[7] I. A. Qattan *et al.*, Phys. Rev. Lett. **94**, 142301 (2005).

[8] M.K. Jones *et al.*, Phys. Rev. Lett. **84**, 1398 (2000).

[9] O. Gayou *et al.*, Phys. Rev. Lett. **88**, 092301 (2002).

[10] O. Gayou *et al.*, Phys. Rev. C **64**, 038202 (2001).

[11] V. Punjabi *et al.* Phys. Rev. C**71** (2005) 055202.

[12] P.G. Blunden, W. Melnitchouk, J.A. Tjon, P.R.L. **91** 142304 (2003).

[13] Y. M. Bystritskiy, E. A. Kuraev, and E. Tomasi-Gustafsson, hep-ph/0603132.

[14] A. De Rujula, H. Georgi and S.L. Glashow, Phys. Rev. D **12**, 147 (1975); N. Isgur and G. Karl, Phys. Rev. D **18**, 4187 (1978); **19**, 2653 (1979); **20**, 1191 (1979); C. Hayne and N. Isgur, *ibid* **25**, 1944 (1982).

[15] P.L. Chung and F. Coester, Phys. Rev. D **44**, 229 (1991).

[16] M.R. Frank, B.K. Jennings and G.A. Miller, Phys. Rev. C **54**, 920 (1996).

[17] F. Schlumpf, Phys. Rev. D **47**, 4114 (1993).

[18] F. Cardarelli and S. Simula Phys. Rev. C **62**, 65201 (2000).

[19] E. Pace, G. Salme, F. Cardarelli and S. Simula, Nucl. Phys. A **666**&**667**, 33c (2000).

[20] M. De Sanctis, M.M. Giannini, L. Repetto and E. Santopinto, Phys. Rev. C **62**, 25208 (2000).

[21] S. Boffi *et al.*, Eur. Phys. J. A **14**, 17 (2002); S. Boffi *et al.*, hep-ph/0108271 v1 (2001).

[22] G.A. Miller, Phys. Rev. C **68**, 022201(R) (2003).

[23] Franz Gross and Peter Agbakpe, Phys. Rev. C **73**, 015203 (2006).

[24] A. Kvinikhidze and G.A. Miller, Phys. Rev. C **73**, 065203 (2006).

[25] A.V. Belitzky, X. Ji and F. Yuan, hep-ph/0212351 (2003).

[26] S.J. Brodsky, hep-ph/0208158 v1 (2002).

[27] G.A. Miller and M.R. Frank, Phys. Rev. C **65**, 065205 (2002).

[28] A.L. Licht and A. Pagnamenta, Phys. Rev. D **2**, 1150 (1970).

[29] J.J. Kelly, Phys. Rev. C **66**, 065203 (2002).

[30] A. Radyushkin, Phys. Rev. D **58**, 114008 (1998)

[31] A. V. Afanasev, arXiv:hep-ph/9910565.

[32] P. Stoler, Phys. Rev. D **65**, 053013 (2002) [arXiv:hep-ph/0108257].

[33] M. Guidal, M. V. Polyakov, A. V. Radyushkin and M. Vanderhaeghen, Phys. Rev. D **72**,054013 (2005).

[34] M. Diehl, T. Feldmann, R. Jakob and P. Kroll, Eur. Phys. J. C **39**, 1 (2005) [arXiv:hep-ph/0408173].

[35] M. Burkardt, Int. J. Mod. Phys. A**18**, 173 (2003)

[36] X. D. Ji, Phys. Rev. Lett. **78**, 610 (1997), Phys. Rev. D **55**,7114 (1997).

[37] A.I. Akhiezer and M.P. Rekalo, Sov. J. Part. Nucl. **3**, 277 (1974).

[38] R. Arnold, C. Carlson and F. Gross, Phys. Rev. C **23**, 363 (1981).

[39] E. Aprile-Giboni *et al*, NIM **215**, 147 (1943).

[40] L.S. Azhgirey *et al.*, NIM A 538, 431 (2005).

[41] N.E. Cheung *et al.*, NIM A 363, 561 (1995).

[42] I.G. Alekseev *et al.*, NIM A 434, 254 (1999).

[43] E.L. Lomon, Phys.Rev. C **64**, 035204 (2001).

[44] R. Bijker and F. Iachello, Phys, Rev. C **69**, 068201 (2004).